Rapid erosion increases the efficiency of hillslope sediment transport

Emmanuel J. Gabet[1,1], Simon Marius Mudd[2,2], Ryan Wood[3,3], Stuart William David Grieve[4,4], Steven A. Binnie[5,5], and Tibor J. Dunai[6,6]

[1]San José State University
[2]University of Edinburgh
[3]San Jose State University
[4]Queen Mary University of London
[5]Universität zu Köln
[6]Universtiät zu Köln

November 30, 2022

Abstract

The shape of soil-mantled hillslopes is typically attributed to erosion rate and the transport efficiency of the various processes that contribute to soil creep. While climate is generally hypothesized to have an important influence on soil creep rates, a lack of uniformity in the measurement of transport efficiency has been an obstacle to evaluating the controls on this important landscape parameter. We addressed this problem by compiling a data set in which the transport efficiency has been calculated using a single method, the analysis of hilltop curvatures using 1-m LiDAR data, and the erosion rates have also been determined via a single method, in-situ ¬cosmogenic 10Be concentrations. Moreover, to control for lithology, we chose sites that are only underlain by resistant bedrock. The sites span a range of erosion rates (6 – 922 mm/kyr), mean annual precipitation (39 – 320 cm/yr), and aridity index (0.08 – 1.38). Surprisingly, we find that hilltop curvature varies with the square root of erosion rate, whereas previous studies predict a linear relationship. In addition, we find that the inferred transport coefficient also varies with the square root of erosion rate but is insensitive to climate. We explore various mechanisms that might link the transport coefficient to the erosion rate and conclude that present theory regarding soil-mantled hillslopes is unable to explain our results and is, therefore, incomplete. Finally, we tentatively suggest that processes occurding in the bedrock (e.g., fracture generation) may play a role in the shape of hillslope profiles at our sites.

Hilltop Curvature Increases with the Square Root of Erosion Rate

2

E. J. Gabet[1], S. M. Mudd[2], R. W. Wood[1], S. W. D. Grieve[3], S. A. Binnie[4], T. J. Dunai[4]

4

[1] Department of Geology, San Jose State University, San Jose, California, 95192, USA.
[2] School of Geosciences, University of Edinburgh, Edinburgh, UK, EH9 3FE.
[3] School of Geography, Queen Mary University of London, London, UK, E1 4NS.
[4] Institute for Geology and Mineralogy, University of Cologne, Germany, 50674.

9

Corresponding author: Emmanuel Gabet (manny.gabet@sjsu.edu)

11

Key Points:

- Hilltop curvature at our sites does not vary linearly with erosion rate, as predicted by theory

- The inferred transport coefficient appears to be insensitive to climate

- Processes affecting the underlying bedrock may control the shape of soil-mantled hillslopes

18

Abstract

The shape of soil-mantled hillslopes is typically attributed to erosion rate and the transport efficiency of the various processes that contribute to soil creep. While climate is generally hypothesized to have an important influence on soil creep rates, a lack of uniformity in the measurement of transport efficiency has been an obstacle to evaluating the controls on this important landscape parameter. We addressed this problem by compiling a data set in which the transport efficiency has been calculated using a single method, the analysis of hilltop curvatures using 1-m LiDAR data, and the erosion rates have also been determined via a single method, *in-situ* cosmogenic ^{10}Be concentrations. Moreover, to control for lithology, we chose sites that are only underlain by resistant bedrock. The sites span a range of erosion rates (6 – 922 mm/kyr), mean annual precipitation (39 – 320 cm/yr), and aridity index (0.08 – 1.38). Surprisingly, we find that hilltop curvature varies with the square root of erosion rate,

31 whereas previous studies predict a linear relationship. In addition, we find that the inferred

32 transport coefficient also varies with the square root of erosion rate but is insensitive to

33 climate. We explore various mechanisms that might link the transport coefficient to the

34 erosion rate and conclude that present theory regarding soil-mantled hillslopes is unable to

35 explain our results and is, therefore, incomplete. Finally, we tentatively suggest that

36 processes occurding in the bedrock (e.g., fracture generation) may play a role in the shape of

37 hillslope profiles at our sites.

38 **Index Terms: 1826, 1819, 1862**

39 **1. Introduction**

40   On soil-mantled surfaces too gentle for significant landsliding, particles are primarily

41 transported downslope by soil creep. Soil creep is a general term for the cumulative effect of

42 myriad individual processes that locally disturb soil, such as the freezing and thawing of pore

43 water [*Anderson et al.*, 2013], shrink-swell cycles [*Carson and Kirkby*, 1972], dry ravel

44 [*Anderson et al.*, 1959; *Gabet*, 2003], burrowing by animals [*Gabet et al.*, 2003], and tree

45 throw [e.g., *Denny and Goodlett*, 1956]. Culling [1963] proposed that the rate of soil creep

46 (q_s; L^2/T) is linearly proportional to hillslope gradient, S (L/L), such that

47          $$q_s = DS \qquad\qquad\qquad (1)$$

48 where D (L^2/T) is a sediment transport coefficient. The sediment transport coefficient, D, is a

49 measure of the efficiency of the various soil creep processes, and its magnitude sets the pace

50 for hillslope evolution [e.g., *Fernandes and Dietrich*, 1997; *Roering et al.*, 1999]. Although a

51 nonlinear relationship between gradient and flux is supported by topographic analysis

52 [*Andrews and Bucknam*, 1987; *Grieve et al.*, 2016; *Hurst et al.*, 2012; *Roering et al.*, 1999]

53   and physical simulations [*Gabet*, 2003; *Roering et al.*, 2001b], this relationship reduces to

54   Eqn. (1) on slopes < 20° [*Hurst et al.*, 2012].

55   Our understanding of the controls on *D* for a particular landscape is limited. Because

56   soil creep processes are typically climatically controlled, either directly (e.g., freeze-thaw) or

57   indirectly through climate's effect on the distribution of the biota, temperature and

58   precipitation are expected to have a dominant role in the transport efficiency of soil creep

59   [e.g., *Dunne et al.*, 2010; *Hanks*, 2000; *Pelletier et al.*, 2011]. Indeed, Hurst et al. [2013] and

60   Richardson et al. [2019] found that *D* increases with mean annual precipitation, albeit

61   weakly; the latter also found that *D* increases with the aridity index, which is the ratio

62   between precipitation and evapotranspiration [*Trabucco and Zomer*, 2019]. In contrast, Ben-

63   Asher et al. [2017] concluded that transport efficiency decreases with precipitation, although

64   this result was based on a small data set. Soil thickness [*Furbish et al.*, 2009; *Heimsath et al.*,

65   2005] and soil texture [*Furbish et al.*, 2009], as well as underlying lithology [*Hurst et al.*,

66   2013], may also be important factors. A lack of uniformity in measuring *D*, however, has

67   been an obstacle in investigating the effect of these various factors.

68   Determining the controls on the transport coefficient is important for a variety of

69   reasons. Because many landscapes are soil-mantled, not affected by overland flow, and too

70   gentle for significant landsliding, Eqn. (1) and its nonlinear counterpart are thought to offer a

71   complete description (or nearly so) of sediment transport across much of the Earth's surface.

72   Moreover, assuming steady-state topography, combining Eqn. (1) with a statement of mass

73   conservation yields

74    $$C_{HT} = -\frac{E}{D}\left(\frac{\rho_s}{\rho_r}\right) \tag{2}$$

75   where E is the erosion rate (L/T), C_{HT} (1/L) is the two-dimensional curvature (i.e., the

76   Laplacian of elevation) of a hill's ridgecrest, and ρ_s and ρ_r are the density (L^3/T) of soil and

77   rock, respectively [*Roering et al.*, 2007]. With this equation (and its nonlinear version), D

78   and E are both assumed to be independent variables: E is controlled by the rate at which the

79   lower boundary is lowered (e.g., via river incision in response to uplift), and D is controlled

80   by the intensity of the various soil creep processes. According to this theory, the profile of a

81   hillslope adjusts itself such that its curvature satisfies Eqn. (2) [*Culling*, 1963; *Gilbert*, 1909].

82   Therefore, understanding the controls on the transport efficiency should provide insight into

83   hillslope form. In addition, studies have used Eqn. (1) and its nonlinear version to model the

84   degradation of fault scarps to estimate earthquake recurrence interval [e.g., *Hanks and*

85   *Schwartz*, 1987], and the results are sensitive to the value of the transport coefficient. Finally,

86   understanding the role of the various factors on D is important as geologists attempt to infer

87   erosion rates based on topographic analyses [*Hurst et al.*, 2012].

88   **2. Methods**

89   2.1. Site selection and descriptions

90   Appropriate sites were limited to watersheds which had both LiDAR and cosmogenic

91   [10]Be data sets. The [10]Be data came from a global compilation [*Harel et al.*, 2016], and the

92   associated LiDAR data were acquired from the OpenTopography (http://opentopo.sdsc.edu)

93   and USGS (https://viewer.nationalmap.gov) platforms. LiDAR data with spatial resolutions

94   coarser than 1-m cannot accurately resolve ridgeline curvatures in all settings [*Grieve et al.*,

95   2016] and so any sites without 1-m resolution data were excluded from the analysis. Because

96   ridgeline curvatures were used to estimate D (see below), only watersheds that appeared to

97   be in topographic steady-state were chosen. For example, watersheds with clear knickpoints

98   or with asymmetrical ridges were avoided, as well as steep watersheds advancing into low-

99   relief surfaces. Simulations of hillslope evolution suggest that hillslopes with declining

100   erosion rates adjust so quickly that they are difficult to differentiate from steady state

101   hillslopes; furthermore, hillslopes experiencing accelerated uplift only preserve the signature

102   of changing erosion rates for tens of thousands of years [*Mudd*, 2017]. Therefore, by

103   avoiding areas with obvious signs of landscape transience, we are less likely to find ridgeline

104   curvatures reflective of transient conditions. Thirty sites from six regions in the United States

105   met our criteria: the Olympic Peninsula (WA) [*Belmont et al.*, 2007], the Feather River area

106   (CA) [*Hurst et al.*, 2012; *Riebe et al.*, 2001; *Saucedo and Wagner*, 1992], the San Gabriel

107   Mountains (CA) [*DiBiase et al.*, 2010], Yucaipa Ridge (CA) [*Binnie et al.*, 2007], the Idaho

108   Plateau (ID) [*Wood*, 2013], and the Blue Ridge Mountains (VA) [*Duxbury*, 2009] (Figure 1) .

109   Some of the regions (e.g., the San Gabriel Mountains) had ^{10}Be data for sites not covered by

110   available LiDAR data and, thus, their full data-sets could not be used. Climatic data for these

111   sites were obtained from the 800-m resolution PRISM model [*PRISM*, 2014], which provides

112   recent (1981 – 2010) 30-yr means for annual precipitation (MAP) and annual temperature

113   (MAT) (Table 1). The aridity index for the sites was determined from Trabuco and Zomer

114   [2019]. While these data are for the modern climate, we assume that they are representative

115   (at least in a relative sense) of the climate state over the time-scale of the erosion rates

116   measured with ^{10}Be (i.e., 10^3 - 10^5 yrs). To control for rock strength, we chose sites underlain

117   by lithologies known to be resistant to erosion: plutonic and metamorphic bedrock [e.g.,

118   *Gabet*, 2020; *Hack*, 1973] (Table 1).

119   2.2. Erosion rate calculations

120   To ensure a consistent method for calculating erosion rates, they were determined

121 from ^{10}Be concentrations in detrital quartz grains (Table 1). For five of the study regions,

122 published ^{10}Be concentrations were used to calculate basin-scale erosion rates. For the Idaho

123 Plateau sites, ^{10}Be concentrations were measured from soil and fluvial sediment samples

124 collected for this study (see below). For all six study regions, erosion rates were calculated

125 from the ^{10}Be concentrations using a single algorithm [*Mudd et al.*, 2016].

126   A full description of the Idaho Plateau field area can be found in Wood [2013].

127 Ridgetop and basin-scale denudation rates were determined by measuring cosmogenic ^{10}Be

128 concentrations in quartz [*Brown et al.*, 1995; *Granger et al.*, 1996]. The ridgetop rates were

129 determined from soil samples taken from the top 20 cm of the regolith at three sites. For the

130 basin-scale erosion rates, fluvial sediment was taken from three 1st-order streams. Pure quartz

131 fractions from the crushed and sieved (250-710 µm) and magnetically separated samples

132 were obtained using published procedures [*Kohl and Nishiizumi*, 1992; *Mifsud et al.*, 2013].

133 ICP-OES analysis of purity was undertaken on splits of the etched quartz. Samples were

134 spiked with ~200 µg of a commercial Be carrier (Scharlab Berylium ICP standard solution)

135 and prepared as AMS targets at the University of Cologne using a standard sample

136 preparation method [2015]. The samples were prepared alongside a reagent blank; ^{10}Be

137 concentrations following blank subtraction are reported in Table 2. Blank corrections are <2

138 %, except for sample S2, for which the correction is <5 %. Samples were measured on

139 CologneAMS [*Dewald et al.*, 2013] and normalized to reference standards [2007].

140 Uncertainties in the concentrations are estimated by propagating the uncertainties of the

141   AMS measurements and mass of Be added during spiking (estimated 1σ uncertainty of 1%)

142   of both the samples and the blank.

143   [10]Be concentrations were converted to denudation rates with the CAIRN software

144   package, which accounts for topographic shielding and snow shielding [*Mudd et al.*, 2016].

145   We calculated snow shielding by first fitting a bilinear trend in snow water equivalent (SWE)

146   as a function of elevation based on regional climate data from the National Oceanic and

147   Atmospheric Association [*NOAA*, 2016] and following Kirchner et al. [2014]. SWE averages

148   were converted to snow shielding values by assuming that snow reduces production solely by

149   spallation [*Mudd et al.*, 2016]. Snow shielding is highly uncertain because of the difficulty of

150   estimating the average SWE over the timescales of $10^3 - 10^4$ years. We calculated

151   denudation rates with no snow shielding to assess the sensitivity of denudation rate to snow

152   thickness and found that, without accounting for snow, denudation rate estimates could be as

153   much as 15% higher (for sample S3) but, for most samples, the differences were less than

154   10%. Uncertainties from analytical error and from uncertainties in production scaling and

155   shielding are presented in Table 1 [*Mudd et al.*, 2016].

156   2.3. Transport Coefficient Calculations

157   Direct estimates of the transport efficiency by field measurements of sediment fluxes

158   over the relevant time and spatial scales across a range of landscapes are impractical. Instead,

159   along ridgelines, where slopes are gentle and soil creep is well described by Eqn. (1), the

160   transport coefficient can be calculated by rewriting Eqn. (2) as

$$D = -\left(\frac{E}{C_{HT}}\right)\left(\frac{\rho_r}{\rho_s}\right)$$

161   (3).

162   The ratio ρ_r/ρ_s was assumed to be 2 [*Hurst et al.*, 2012]; this value is probably only

163   approximately correct for each of our sites and likely varies by ±25%. Ridgeline curvatures

164   were calculated from a 1-m LiDAR DEM for each site using a six-term polynomial function

165   to fit the elevation data within a circular sliding window with a diameter of 14 m. A value of

166   14 m for the analysis window was chosen based on sensitivity analyses presented in Grieve

167   et al. [2016] which followed the method for identifying the optimal window diameter

168   described in Roering et al. [2010] and Hurst et al. [2012].

169   The second derivative of the polynomial function at the window's center is that cell's

170   two-dimensional curvature. Because topographic noise could produce outliers, the median of

171   the curvatures along each watershed's ridgeline was used in our analyses [*Hurst et al.*, 2012].

172   The average slopes (± 1σ) along the ridgelines, determined as the first derivative of the

173   polynomial function, ranged from 0.5 ± 3° (Blue Ridge Mtns) to 9 ± 6° (Yucaipa Ridge),

174   thereby validating the use of Eqn. (1). Note that, even at the steepest site along Yucaipa

175   Ridge, nearly 95% of the area analyzed had slopes < 20°. Finally, an automated procedure

176   was used to detect the presence of bedrock outcrops along the ridgelines [*Milodowski et al.*,

177   2015] to confirm that the sites were mantled with soil. One Yucaipa Ridge site had 75% soil-

178   cover and the other had 90% soil-cover; the soil-cover at the other sites ranged from 97 to

179   100%. Observations of Google Earth$^{\text{TM}}$ imagery supported these estimates.

180   2.3 Additional Data

181   The dataset described above was supplemented with data selected from a compilation

182   presented in Richardson et al. [2019] (Table 1). From this compilation, four sites met our

183   criteria: the ridgelines were symmetrical, transport coefficients were estimated by analyzing

184   ridgetop curvatures from 1-m LiDAR data, erosion rates were determined with cosmogenic

185 [10]Be, and the soils were derived from resistant lithologies (Table 1). The only difference is

186 that Richardson et al. used a 15-m window for their curvature analysis whereas our study

187 used a 14-m window; we consider this difference to be insignificant. With the combined

188 datasets, the sites represent a range of erosion rates from 6 to 922 mm/kyr, a range of mean

189 annual precipitation from 39 to 320 cm/yr, a range of mean annual temperature from 2 to 15°

190 C, and range of aridity index from 0.08 to 1.38 (Table 1).

191   2.4 Correcting for Grid Resolution

192   As erosion rates increase, ridgelines become sharper, which could potentially weaken

193 the ability to accurately measure curvature given a fixed grid resolution. In particular, this

194 grid-resolution effect could lead to an increasing underestimate of curvature as ridgelines

195 sharpen with increasing erosion rates, thereby artificially introducing a positive relationship

196 between D and E. To correct for this potential artefact, we performed an analysis in which we

197 compared the estimates of the transport efficiency with those from idealized one-dimensional

198 (1D) hillslopes. We assumed our ridges can be approximated as one-dimensional because

199 curvature perpendicular to ridgelines far exceeds curvature parallel to our ridgelines.

200   To begin, we solved for the elevation of an idealized 1D hillslope by assuming that a

201 nonlinear sediment flux law describes sediment transport on our hillslopes [e.g., *Andrews*

202 *and Bucknam*, 1987; *Roering et al.*, 1999]

203
$$q_s = -\frac{D\frac{\partial z}{\partial x}}{1-\left(\left|\frac{\partial z}{\partial x}\right|\middle/S_c\right)^2} \tag{4}$$

204 where q_s is sediment flux (m^2/yr), D is the sediment transport coefficient (m^2/yr), z is the

205 surface elevation, x is a horizontal distance, and S_c is a critical slope angle. As noted earlier,

206   this equation reduces to Eqn. (1) at gentle slopes. Inserting Eqn. (4) into a statement of mass

207   conservation and solving it under steady-state conditions yields an expression for the

208   elevation of a hillslope [*Roering et al.*, 2001a]:

209    $$z = -\frac{S_c^2}{2\beta}\left[\sqrt{D^2 + \left(\frac{2\beta x}{S_c^2}\right)} - D\ln\left(\frac{S_2}{2\beta}\sqrt{D^2 + \left(\frac{2\beta x}{S_c^2}\right)^2} + \frac{S_c D}{2\beta}\right)\right] + c \quad (5)$$

210   where β is the ratio between rock and soil density multiplied by the erosion rate $((\rho_r/\rho_s)*E)$

211   and c is a constant that sets the absolute elevation of the hillslope profile. At the divide ($x = 0$

212   m), the curvature is equal to:

213    $$\left(\frac{d^2 z}{dx^2}\right)_{HT} = -\frac{\beta}{D} \qquad (6).$$

214   As described earlier, curvature at each site was measured from gridded 1-m

215   topographic data. To mimic this procedure on the synthetic hillslope, we solved Eqn. (5) on a

216   grid of points with a spacing of 1 m. Random noise was then imposed on each gridded data

217   point from a uniform distribution ranging from -0.1 to 0.1 m, which is a conservative

218   estimate of vertical error in typical airborne LiDAR data. As with the real landscapes, a 2nd-

219   order polynomial equation was fitted across the ridgetop over a 14-m window and the

220   curvature was calculated at the center node.

221   However, in any gridded topography, the highest true elevation of the ridge may not

222   be located exactly on the grid sampling point. The exact location of the ridge may be offset

223   from the highest gridded pixel by up to half a pixel width. In Eqn. (5), the ridge is located at

224   x = 0 meters, but to account for the possibility that the ridgeline does not correspond to the

225   highest pixel, we allowed the gridded points to shift laterally by 0.5 m to produce an offset

226   between the center point in the gridded data and the ridgeline.

227　　　　For each study site (Table 1), the values of β and S_c were calculated using the erosion

228　　rate and measured curvature to produce idealized ridgetop profiles. Random noise was then

229　　applied to the profile, the grid was shifted, and the 'synthetic' curvature was calculated from

230　　the fitted 2nd-order polynomial. This process was repeated with variations in D until the

231　　synthetic curvature matched the curvature measured from the topographic data. We

232　　performed 250 iterations of adding random noise to a profile centered on the hilltop, and 250

233　　iterations of random noise to a profile centered 0.5 m from the hilltop. These calculations

234　　resulted in 500 values for the sediment transport coefficient that account for (1) sampling a

235　　continuous hillslope with gridded data, (2) random noise from the DEM, and (3) a potential

236　　mismatch between the actual location of the hillcrest and the highest pixel along the 1D ridge

237　　in the DEM.

238

239　**3. Results**

240　　　　We find that the 'raw' hilltop curvature (i.e., uncorrected for grid-scale effects) is

241　　strongly correlated with the approximate square root of erosion rate: $C_{HT} \propto E^{0.48}$ (Figure 2).

242　　The 'corrected' hilltop curvature is also correlated with erosion rate although the exponent in

243　　the regression increases to 0.53 (Figure 3). In addition, the transport coefficient (calculated

244　　from the corrected hilltop curvatures) varies with erosion rate, whereby $D \propto E^{0.47}$ (Figure 4).

245　　　　 The transport efficiency is not correlated with any of the climate parameters (Figure

246　　5) nor with the 'effective energy and mass transfer' variable (plot not shown), a parameter

247　　which incorporates both MAT and MAP to represent the influence of climate on soil

248　　processes [*Rasmussen and Tabor*, 2007].

249   **4. Discussion**

250   Our results indicate that, at the sites we examined, erosion rate appears to have a

251   dominant control on the efficiency of sediment transport. The apparent role of erosion rate on

252   the efficiency of hillslope sediment transport and the insignificance of climate is unexpected

253   considering that others have found a climatic influence on the value of *D* [*Hurst et al.*, 2013;

254   *Richardson et al.*, 2019]. In contrast to our results, Richardson et al. [2019] compiled erosion

255   rate and transport coefficient data from studies which used a variety of techniques to estimate

256   these values, and their data included sites in a range of lithologies as well as from regions

257   with a greater range in precipitation. As a result, their larger data set may be better suited for

258   detecting an underlying climatic influence.

259   To explore how transport efficiency might increase with erosion rate, the factors

260   contributing to soil creep can be assessed with two approaches. For discrete, intermittent

261   large-scale soil creep events (e.g., tree throw), the transport efficiency can be calculated as

262

263         $$D = f_e \overline{V} \overline{d} \tag{7}$$

264

265   where f_e is the frequency of events per unit area ($T^{-1}L^{-2}$), $\overline{V}$ is the average volume (L^3) of soil

266   displaced with each event, and $\overline{d}$ is the average distance (L) that volume of soil is displaced

267   [*Gabet*, 2000]. For example, in the case of tree throw, the transport coefficient will depend

268   on the number of toppled trees over a period of time, the average volume of soil in the root

269   plates, and the distance that the root plates are displaced [*Gabet et al.*, 2003]. We are not

270   aware of any reason why any of these three factors would increase with erosion rate. Indeed,

271   in the case of bioturbation, $\overline{V}$ and f_e might be expected to *decrease*. For example, because

272   soils tend to be thinner where erosion rates are high [e.g., *Gabet et al.*, 2015], the volume of

273   soil available for transport by three throw should decrease. In addition, the frequency of

274   bioturbation might be expected to decrease in rapidly eroding landscapes because of lower

275   plant biomass [*Milodowski et al.*, 2014].

276   For dilational creep processes in which soil particles are lofted up and then settle

277   down due to gravity, *D* can be expressed as [*Furbish et al.*, 2009]

278

$$D = kRhN_a \overline{\left(1 - \frac{P}{P_m}\right)^2} \cos^2 \theta \qquad (8)$$

280

281   where *k* is an empirically determined dimensionless constant that accounts for particle shape

282   and the relationship between mean free path length and the vertical displacement of particles,

283   *R* is particle radius (L), *h* is soil thickness (L), *P* is particle concentration ($L^3 L^{-3}$), P_m is the

284   maximum value of *P*, N_a is the particle activation rate (T^{-1}), θ is the hillslope angle (°) (equal

285   to zero at the ridgecrest), and the overbar signifies vertically averaged quantities. The particle

286   concentration (a function of soil bulk density) is not likely to be dependent on erosion rate to

287   a significant degree and, if it is, the term in parentheses would likely decrease with increasing

288   erosion rate, thereby suppressing the value of *D*. Because soils are thinner in rapidly eroding

289   landscapes [e.g., *Gabet et al.*, 2015], variations in soil thickness also cannot account for the

290   increase in transport efficiency with erosion rate; indeed, the inverse relationship between

291   soil thickness and erosion rate should lead to an inverse relationship between *D* and *E*, the

292   opposite of what we have found. With respect to particle activation rate, we are not aware of

293   any studies that have correlated this variable with erosion rate; however, because rapidly

294   eroding hillslopes tend to have thinner and more exposed soils [e.g., *Gabet et al.*, 2015], the

295   particle activation rate in these landscapes could potentially be higher, which could lead to an

296   increase in *D* with *E*. For example, a decrease in vegetation biomass with increasing erosion

297   rate [*Milodowski et al.*, 2014] could leave the soil surface more vulnerable to raindrop impact

298   [*Dunne et al.*, 2010]. Nevertheless, as noted above, a reduction in biomass might also be

299   expected to damp bioturbation, thereby reducing the transport efficiency.

300   The final variable from Eqn. (8) to be explored is particle diameter, *R*. Previous

301   studies have documented an increase in particle diameter with erosion rate [*Attal et al.*, 2015;

302   *Riebe et al.*, 2015]. Where erosion is slow, particles are exposed to weathering processes for

303   longer periods of time because of longer soil residence times and, as a result, particles

304   become smaller [e.g., *Mudd and Yoo*, 2010]. In Eqn. (8), particle size is a factor in the

305   transport coefficient because it controls the mean free path of particles in a soil creeping by

306   dilational processes [*Furbish et al.*, 2009]. Although field data from Neeley et al. [2019]

307   suggest that coarser soils have a higher transport coefficient, laboratory experiments have

308   demonstrated that, for the same input of energy, coarse-grained soils will creep faster than

309   fine-grained soils [Supplement to *Deshpande et al.*, 2020]. In addition, of the various factors

310   that could affect the rate of soil creep, particle size is the one with the most potential to vary

311   by multiple orders-of-magnitude between watersheds eroding at different rates [*Marshall and*

312   *Sklar*, 2012]. For example, while the data are limited, particle radius along a ridgeline

313   increases with erosion rate at the Feather River site (Figure 6).

314   While particle size is a potential candidate for explaining the relationship between

315   transport efficiency and erosion rate found here, this hypothesis raises some perplexing

316   issues. First, whereas the relationship between particle size and erosion rate is likely to be

317   constant within a single region, one would expect them to vary between regions according to

318   climate and lithology (although we tried to control for rock strength, variations in texture, for

319   example, could affect particle size). However, despite the expected regional variations in

320   these factors, the sites fall along the same *D* vs. *E* trendline (Figure 3). Second, because the

321   more rapid weathering rates in wetter climates should lead to smaller soil particles [*Marshall*

322   *and Sklar*, 2012], the transport coefficient should decrease in wetter climates. However, we

323   find no relationship between mean annual precipitation and *D* (Figure 5).

324   Another potential explanation may be that the transport efficiency is sensitive to slope.

325   Landscapes that are eroding quickly are generally steeper than those that are eroding more

326   slowly. For example, the slopes at the ridgecrests (S_{HT}) at our sites increase with the

327   approximate square root of erosion rate (Figure 7). Some property of the soil (e.g., its

328   resistance to disturbance) may be affected by the gradient such that its transport efficiency

329   increases on steeper slopes (P. Richardson, pers. comm.). Furbish and Haff [2010] suggest

330   that the rate at which soil is mobilized might also increase with slope. To explore the

331   consequences of a slope-dependent transport coefficient, we define a new variable, D_s (L^2/T)

332        $D_s = KS$ (10)

333   such that

334        $q_s = D_s S$ (11a)

335   or

336        $q_s = KS^2$ (11b)

337   where K (L^2/T) is a constant with the same properties as *D*. Inserting Eqn. (11b) into a

338   statement of mass conservation

$$339 \qquad \rho_r \frac{dz}{dt} = -\rho_s \frac{dq_s}{dx} \tag{12}$$

340 and integrating twice assuming steady state ($dz/dt = E$) and $\rho_r/\rho_s = 2$ yields

$$341 \qquad E = KCS/2 \tag{13a}.$$

342 To specify that this relationship is applied to the hilltops, we rewrite it as

$$343 \qquad E = KC_{HT}S_{HT}/2 \tag{13b}.$$

344 Thus, the assumption that the transport coefficient increases linearly with slope implies a

345 linear relationship between the erosion rate and the product of curvature and slope. Indeed, a

346 power-law regression between the two yields an exponent of unity, offering support for the

347 hypothesis that the transport coefficient is slope-dependent (Figure 8). However, because

348 slope and curvature are linearly related along a parabolic curve, Eqn. (13b) is functionally

349 equivalent to $E \propto C^2$ or $C \propto E^{1/2}$, which is the original relationship presented in Figure 3. In

350 other words, the linear relationship between E and $C_{HT}S_{HT}$ may simply be a mathematical

351 artefact, and the sediment flux relationship represented by Eqn. (11b) would need to be

352 validated independently. Finally, note that Eqn. (11b) is quite different from the nonlinear

353 sediment flux equation proposed elsewhere [*Andrews and Bucknam*, 1987; *Gabet*, 2003;

354 *Roering et al.*, 1999], particularly at lower slopes (Figure 9).

355   The lack of a clear and robust mechanistic link between D and E, as well as the square

356 root dependency of the hilltop curvature on erosion rate when Eqn. (2) predicts a linear

357 relationship, suggests that the present theory explaining the profile of soil-mantled hillslopes

358 is incomplete. We tentatively propose that, in resistant lithologies, hillslope curvature may be

359 partially, if not mostly, controlled by processes occuring within the bedrock, rather than the

360 soil. Indeed, in an eroding landscape, the soil on a hill is just a thin mantle covering a much

361 larger bedrock mass; the shape of the hill, therefore, should reflect the shape of the

362   underlying bedrock and the processes acting within it [e.g., *Rempe and Dietrich*, 2014].

363   However, the absence of any climatic influence in our results suggests that these bedrock

364   processes are not associated with the typical chemical and physical weathering processes;

365   instead, they are likely related to a more universal mechanism. Recent work has begun

366   investigating how, even in soil-mantled landscapes, the generation of fractures in bedrock by

367   topographic stresses may exert an important influence on landform shape [e.g., *Clair et al.*,

368   2015; *Pelletier*, 2017; *Slim et al.*, 2015]. However, whereas the regional tectonic stress is an

369   important contributor to topographic stresses [e.g.,*Clair et al.*, 2015; *Miller and Dunne*,

370   1996], the tectonic stress regime varies widely between our sites. For example, the regional

371   stresses are compressional in the San Gabriel Mountains but extensional in the Wasatch

372   Mountains and the Feather River study area [*Heidbach et al.*, 2016; *Wakabayashi and*

373   *Sawyer*, 2000]. Therefore, the alignment of these sites along the same trendline (Figure 2)

374   suggests that our present understanding of rock fracture by topographic stresses is unable to

375   explain our results.

376   One potential avenue for further investigations may be an examination of the time-

377   dependent nature of fracture growth. At high erosion rates, near-surface bedrock is

378   rejuvenated more quickly, thereby limiting the fracture density. In contrast, in environments

379   where the erosion rate is slower and the rejuvenation of the surface occurs less frequently, the

380   near-surface bedrock may have a higher fracture density as it accumulates damage over time.

381   The relationship found here between hilltop curvature and erosion rate, therefore, may be

382   related to the strength of the underlying rock mass in a way that is not yet understood. As a

383   preliminary test of this idea, we analyzed the data from four sites that met our criteria but

384   were underlain by presumably weak lithologies, sedimentary bedrock or highly sheared

385   metamorphic bedrock [*Perron et al.*, 2012; *Richardson et al.*, 2019]. A comparison of the

386   hilltop curvatures between our original data-set consisting of resistant rocks and the data

387   from the weaker lithologies suggests that, for the same erosion rate, the weaker bedrock

388   forms hilltops with lower curvatures (Figure 10). While the data set from presumably weak

389   lithologies is limited, it supports our hypothesis that weaker bedrock is associated with lower

390   curvatures. Although one might argue that the lower curvatures seen in hillslopes underlain

391   by weaker lithologies could be a result of higher transport efficiencies, a clear mechanistic

392   link between bedrock strength and transport efficiency is lacking (see below), especially

393   considering that most soil creep processes (e.g., tree throw) do not appear to be limited by

394   soil texture.

395   If bedrock processes have an important influence on hillslope form, then hilltop

396   curvature cannot be used for estimating the transport coefficient, at least in landscapes

397   underlain by resistant rock. This limitation might explain why we were unable to detect any

398   climatic influence on D, in contrast to compilations that include estimates of D from a variety

399   of techniques [*Hurst et al.*, 2013; *Richardson et al.*, 2019]. In addition, if hillslope form is

400   primarily dependent on the underlying bedrock, estimates of D based on topographic

401   characteristics might be expected to be of different magnitudes than estimates from other

402   techniques. Indeed, in the compilation presented by Richardson et al. [2019], transport

403   coefficients estimated from relief and hilltop curvature are generally 5 – 10 times higher than

404   those estimated from the modeling of scarps for the same aridity index (a factor that was

405   determined to be a control on D) despite the fact that estimates based on scarp evolution were

406   often performed on slopes comprised of unconsolidated sediment, which might be expected

407   to have higher values of D. Therefore, the mismatch between the estimates of the transport

408   coefficient based on topographic metrics and those based on other techniques suggests that

409   some other factor is influencing hillslope shape.

410   **5. Conclusions**

411   The square-root dependency of hilltop curvature on erosion rate challenges the

412   prevailing theory linking soil creep to the shape of soil-mantled hillslopes, which predicts a

413   linear relationship between the two. This dependency could be explained if the transport

414   coefficient also varies with the square root of erosion rate. However, we are unable to

415   propose a robust mechanism linking the transport coefficient to the erosion rate. Given the

416   difficulties in accounting for our results within the standard theory of hillslope evolution, we

417   tentatively propose that in landscapes underlain by resistant lithologies, hillslope curvature is

418   not related to soil creep but is, instead, controlled by processes in the underlying bedrock.

419   Finally, the robust relationship between ridgetop curvature and erosion rate across a

420   range of climatic conditions suggests that the latter can be estimated directly from

421   topographic analysis in rock types similar to those analyzed in this study. However, erosion

422   rates determined with this procedure must incorporate uncertainties in the original ^{10}Be

423   erosion rate measurements, uncertainties in the curvature measurements, and the uncertainty

424   in the regression between C_{HT} and E. Nevertheless, our results have the potential for

425   providing a simple approach for estimating watershed-scale erosion rates through the

426   measurement of hilltop curvatures.

427

431   author nor did any author have an affiliation that could be perceived as having a conflict of

432   interest with respect to the results of this paper. The data supporting the conclusions can be

433   found in the tables and references. This project was partially funded by graduate student

434   research grants from GSA and SJSU. LiDAR elevation data were acquired with a Seed

435   Project from the National Center for Airborne Laser Mapping in the summer of 2011.

436   Software used for analysis was developed under NERC grant NE/J009970/1. We are grateful

437   to J. Pelletier, J. Roering, and P. Richardson for their careful reviews and helpful comments,

438   and D. Furbish for extended and insightful discussions.

439

Data Availability Statement

441   Original data for this research are provided in Tables 1 and 2. Additional data were

442   compiled from Belmont et al. [2007], Binnie et al. [2007], Dibiase et al. [2010], Duxbury

443   [2009], Hurst et al. [2012], Richardson et al. [2019], and Riebe et al. [2001].

References

445   Anderson, H. W., G. B. Coleman, and P. J. Zinke (1959), Summer slides and winter scour,
446   dry-wet erosion in Southern California mountains: U.S.D.A., Forest Service, *Pacific*
447   *Southwest Forest and Range Experiment Station Technical Paper PSW-36*.
448   Anderson, R. S., S. P. Anderson, and G. E. Tucker (2013), Rock damage and regolith
449   transport by frost: An example of climate modulation of the geomorphology of the
450   critical zone, *Earth Surface Processes and Landforms*, *38*(3), 299-316.
451   Andrews, D. J., and R. C. Bucknam (1987), Fitting degradation of shoreline scarps by a
452   nonlinear diffusion model, *Journal of Geophysical Research*, *92*(B12), 12,857-
453   812,867.
454   Attal, M., S. M. Mudd, M. D. Hurst, B. Weinman, K. Yoo, and M. Naylor (2015), Impact of
455   change in erosion rate and landscape steepness on hillslope and fluvial sediments
456   grain size in the Feather River Basin (Sierra Nevada, California), *Earth Surface*
457   *Dynamics*, *2*, 1047-1092.
458   Belmont, P., F. J. Pazzaglia, and J. C. Gosse (2007), Cosmogenic 10Be as a tracer for
459   hillslope and channel sediment dynamics in the Clearwater River, western
460   Washington State, *Earth and Planetary Science Letters*, *264*, 123-135.

461 Ben-Asher, M., I. Haviv, J. J. Roering, and O. Crouvi (2017), The influence of climate and
462   microclimate (aspect) on soil creep efficiency: Cinder cone morphology and
463   evolution along the eastern Mediterranean Golan Heights, *Earth Surface Processes*
464   *and Landforms*, *42*(15), 2649-2662.
465 Binnie, S. A., W. M. Phillips, M. A. Summerfield, and K. Fifield (2007), Tectonic uplift,
466   threshold hillslopes, and denudation rates in a developing mountain range, *Geology*,
467   *35*, 743-746.
468 Binnie, S. A., T. J. Dunai, E. Voronina, T. Goral, S. Heinze, and A. Dewald (2015),
469   Separation of Be and Al for AMS using single-step column chromatography, *Nuclear*
470   *Instruments and Methods in Physics Research Section B: Beam Interactions with*
471   *Materials and Atoms*, *361*, 397-401.
472 Brown, E. T., R. F. Stallard, M. C. Larsen, G. M. Raisbeck, and F. Yiou (1995), Denudation
473   rates determined from the accumulation of in situ-produced 10Be in the Luquillo
474   Experimental Forest, Puerto Rico, *Earth and Planetary Science Letters*, *129*(1-4),
475   193-202.
476 Carson, M. A., and M. J. Kirkby (1972), *Hillslope form and process*, 475 pp., Cambridge
477   University Press, New York.
478 Clair, J. S., S. Moon, W. S. Holbrook, J. T. Perron, C. S. Riebe, S. J. Martel, B. Carr, C.
479   Harman, K. Singha, and D. d. Richter (2015), Geophysical imaging reveals
480   topographic stress control of bedrock weathering, *Science*, *350*, 534-538.
481 Culling, W. E. H. (1963), Soil creep and the development of hillside slopes, *Journal of*
482   *Geology*, *71*, 127-161.
483 Denny, C., and J. Goodlett (1956), Microrelief resulting from fallen trees, *USGS Professional*
484   *Publication*, *288*, 59-68.
485 Deshpande, N., D. J. Furbish, P. Arratia, and D. Jerolmack (2020), The perpetual fragility of
486   creeping hillslopes, *EarthArXiv*, *doi:10.31223/osf.io/qc9jh*.
487 Dewald, A., et al. (2013), CologneAMS, a dedicated center for accelerator mass spectrometry
488   in Germany, *Nuclear Instruments and Methods in Physics Research Section B: Beam*
489   *Interactions with Materials and Atoms*, *294*, 18-23.
490 DiBiase, R. A., K. X. Whipple, A. M. Heimsath, and W. B. Ouimet (2010), Landscape form
491   and millenial erosion rates in the San Gabriel Mountains, CA, *Earth and Planetary*
492   *Science Letters*, *289*, 134-144.
493 Dunne, T., D. V. Malmon, and S. M. Mudd (2010), A rain splash transport equation
494   assimilating field and laboratory measurements, *Journal of Geophysical Research -*
495   *Earth Surface*, *115*(F01001), 1-16.
496 Duxbury, J. (2009), Erosion rates in and around the Shenandoah National Park, VA,
497   determined using analysis of cosmogenic 10Be, MS thesis, 123 pp, University of
498   Vermont.
499 Fernandes, N. F., and W. E. Dietrich (1997), Hillslope evolution by diffusive processes: the
500   timescale for equilibrium adjustments, *Water Resources Research*, *33*(6), 1307-1318.
501 Furbish, D. J., and P. K. Haff (2010), From divots to swales: Hillslope sediment transport
502   across divers length scales, *Journal of Geophysical Research*, *115*(F03001),
503   doi:10.1029/2009JF001576.
504 Furbish, D. J., P. K. Haff, W. E. Dietrich, and A. M. Heimsath (2009), Statistical description
505   of slope-dependent soil transport and the diffusion-like coefficient, *Journal of*
506   *Geophysical Research*, *114*(F00A05), doi:10.1029/2009JF001267.

507   Gabet, E. J. (2000), Gopher bioturbation: Field evidence for nonlinear hillslope diffusion,
508   *Earth Surface Processes and Landforms*, *25*(13), 1419-1428.
509   Gabet, E. J. (2003), Sediment transport by dry ravel, *Journal of Geophysical Research*,
510   *108*(B1), 2050, 2010.1029/2001JB001686.
511   Gabet, E. J. (2020), Lithological and structural controls on river profiles and networks in the
512   northern Sierra Nevada, *Geological Society of America Bulletin*, *132*(3-4), 655-667.
513   Gabet, E. J., O. J. Reichman, and E. Seabloom (2003), The effects of bioturbation on soil
514   processes and sediment transport, *Annual Review of Earth and Planetary Sciences*,
515   *31*, 259-273.
516   Gabet, E. J., S. M. Mudd, D. T. Milodowski, K. Yoo, M. D. Hurst, and A. Dosseto (2015),
517   Local topography and erosion rate control regolith thickness along a ridgeline in the
518   Sierra Nevada, California, *Earth Surface Processes and Landforms*, *40*(13), 1779-
519   1790.
520   Gilbert, G. K. (1909), The convexity of hillslopes, *Journal of Geology*, *17*, 344-350.
521   Granger, D. E., J. W. Kirchner, and R. C. Finkel (1996), Spatially averaged long-term
522   erosion rates measured from in situ-produced cosmogenic nuclides in alluvial
523   sediment, *Journal of Geology*, *104*(3), 249-257.
524   Grieve, S. W. D., S. M. Mudd, and M. D. Hurst (2016), How long is a hillslope?, *Earth
525   Surface Processes and Landforms*, *41*(8), 1039-1054.
526   Hack, J. T. (1973), Stream-profile analysis and stream-gradient index, *Journal of Research of
527   the U.S. Geological Survey*, *1*(4), 421-429.
528   Hanks, T. C. (2000), The age of scarplike landforms from diffusion‐equation analysis,
529   *Quaternary Geochronology: Methods and Applications*, 313-338.
530   Hanks, T. C., and D. P. Schwartz (1987), Morphologic dating of the pre-1983 fault scarp on
531   the Lost River Fault at Doublespring Pass Road, Custer County, Idaho, *Bulletin of the
532   Seismological Society of America*, *77*, 837-846.
533   Harel, M. A., S. M. Mudd, and M. Attal (2016), Global analysis of the stream power law
534   parameters based on worldwide 10Be denudation rates, *Geomorphology*, *268*, 184-
535   196.
536   Heidbach, O., M. Rajabi, K. Reiter, M. Ziegler, and W. Team (2016), World Stress Map
537   Database Release 2016. V. 1.1, edited, GFZ Data Services.
538   Heimsath, A. M., D. J. Furbish, and W. E. Dietrich (2005), The illusion of diffusion: Field
539   evidence for depth-dependent sediment transport, *Geology*, *33*(12), 949-952.
540   Hurst, M. D., S. M. Mudd, R. C. Walcott, M. Attal, and K. Yoo (2012), Using hilltop
541   curvature to derive the spatial distribution of erosion rates, *Journal of Geophysical
542   Research - Earth Surface*, *115*, 1-19.
543   Hurst, M. D., S. M. Mudd, K. Yoo, M. Attal, and R. C. Walcott (2013), Influence of
544   lithology on hillslope morphology and response to tectonic forcing in the northern
545   Sierra Nevada of California, *Journal of Geophysical Research - Earth Surface*, *118*,
546   832-851.
547   Kirchner, P. B., R. C. Bales, N. P. Molotoch, J. Flanagan, and Q. Guo (2014), LiDAR
548   measurement of seasonal snow accumulation along an elevation gradient in the
549   southern Sierra Nevada, California, *Hydrological Earth Systems Science*, *18*, 4261-
550   4275.

551 Kohl, C. P., and K. Nishiizumi (1992), Chemical isolation of quartz for measurement of in-
552   situ -produced cosmogenic nuclides, *Geochimica et Cosmochimica Acta*, *56*(9), 3583-
553   3587.
554 Marshall, J. A., and L. S. Sklar (2012), Mining soil databases for landscape-scale patterns in
555   the abundance and size distribution of hillslope rock fragments, *Earth Surface*
556   *Processes and Landforms*, *37*(3), 287-300.
557 Mifsud, C., T. Fujioka, and D. Fink (2013), Extraction and purification of quartz in rock
558   using hot phosphoric acid for in situ cosmogenic exposure dating, *Nuclear*
559   *Instruments and Methods in Physics Research Section B: Beam Interactions with*
560   *Materials and Atoms*, *294*, 203-207.
561 Miller, D. J., and T. Dunne (1996), Topographic perturbations of regional stresses and
562   consequent bedrock fracturing, *Journal of Geophysical Research*, *101B*, 25,523-
563   525,536.
564 Milodowski, D. T., S. M. Mudd, and E. T. Mitchard (2014), Erosion rates as a potential
565   bottom-up control of forest structural characteristics in the Sierra Nevada Mountains,
566   *Ecology*, *96*(1), 31-38.
567 Milodowski, D. T., S. M. Mudd, and E. T. A. Mitchard (2015), Topographic roughness as a
568   signature of the emergence of bedrock in eroding landscapes, *Earth Surf. Dynam.*,
569   *3*(4), 483-499.
570 Mudd, S. M. (2017), Detection of transience in eroding landscapes, *Earth Surface Processes*
571   *and Landforms*, *42*(1), 24-41.
572 Mudd, S. M., and K. Yoo (2010), Reservoir theory for studying the geochemical evolution of
573   soils, *Journal of Geophysical Research: Earth Surface*, *115*(F03030).
574 Mudd, S. M., M. Harel, M. D. Hurst, S. W. D. Grieve, and S. M. Marrero (2016), The
575   CAIRN method: Automated, reproducible calculation of catchment-averaged
576   denudation rates from cosmogenic radionuclide concentrations, *Earth Surface*
577   *Dynamics*, *4*, 655-674.
578 Neely, A. B., R. A. DiBiase, L. B. Corbett, P. R. Bierman, and M. W. Caffee (2019),
579   Bedrock fracture density controls on hillslope erodibility in steep, rocky landscapes
580   with patchy soil cover, southern California, USA, *Earth and Planetary Science*
581   *Letters*, *522*, 186-197.
582 Nishiizumi, K., M. Imamura, M. W. Caffee, J. R. Southon, R. C. Finkel, and J. McAninch
583   (2007), Absolute calibration of 10be AMS standards, *Nuclear Instruments and*
584   *Methods in Physics Research Section B: Beam Interactions with Materials and*
585   *Atoms*, *258*(2), 403-413.
586 NOAA (2016), National Center for Environmental Information, edited.
587 Pelletier, J. D. (2017), Quantifying the controls on potential soil production rates: a case
588   study of the San Gabriel Mountains, California, *Earth Surf. Dynam.*, *5*(3), 479-492.
589 Pelletier, J. D., et al. (2011), Calibration and testing of upland hillslope evolution models in a
590   dated landscape: Banco Bonito, New Mexico, *Journal of Geophysical Research:*
591   *Earth Surface*, *116*(F4).
592 Perron, J. T., P. W. Richardson, K. L. Ferrier, and M. Lapotre (2012), The root of branching
593   river networks, *Nature*, *492*, 100-103.
594 PRISM (2014), PRISM Climate Group, edited.

595 Rasmussen, C., and N. Tabor (2007), Applying a quantitative pedogenic energy model across
596   a range of environmental gradients, *Soil Science Society of America Journal*, *71*(6),
597   1719-1729.
598 Rempe, D. M., and W. E. Dietrich (2014), A bottom-up control on fresh-bedrock topography
599   under landscapes, *Proceedings of the National Academy of Sciences*, *111*(18), 6576-
600   6581.
601 Richardson, P. W., J. T. Perron, and N. D. Schurr (2019), Influences of climate and life on
602   hillslope sediment transport, *Geology*, *47*, 423-426.
603 Riebe, C. S., J. W. Kirchner, D. E. Granger, and R. C. Finkel (2001), Minimal climatic
604   control on erosion rates in the Sierra Nevada, California, *Geology*, *29*(5), 447-450.
605 Riebe, C. S., L. S. Sklar, C. E. Lukens, and D. L. Shuster (2015), Climate and topography
606   control the size and flux of sediment produced on steep mountain slopes, *Proceedings*
607   *of the National Academy of Sciences*, *112*(51), 15574-15579.
608 Roering, J. J., J. W. Kirchner, and W. E. Dietrich (1999), Evidence for non-linear, diffusive
609   sediment transport on hillslopes and implications for landscape morphology, *Water*
610   *Resources Research*, *35*(3), 853-870.
611 Roering, J. J., J. W. Kirchner, and W. E. Dietrich (2001a), Hillslope evolution by nonlinear,
612   slope-dependent transport: steady state morphology and equilibrium adjustment
613   timescales, *Journal of Geophysical Research*, *106*(B8), 16499-16513.
614 Roering, J. J., J. T. Perron, and J. W. Kirchner (2007), Functional relationships between
615   denudation and hillslope form and relief, *Earth and Planetary Science Letters*,
616   *264*(1), 245-258.
617 Roering, J. J., J. W. Kirchner, L. S. Sklar, and W. E. Dietrich (2001b), Hillslope evolution by
618   nonlinear creep and landsliding: An experimental study, *Geology*, *29*(2), 143-146.
619 Roering, J. J., J. Marshall, A. M. Booth, M. Mort, and Q. Jin (2010), Evidence for biotic
620   controls on topography and soil production, *Earth and Planetary Science Letters*,
621   *298*, 183-190.
622 Saucedo, G. J., and D. L. Wagner (1992), Geologic map of the Chico quadrangle, California,
623   Division of Mines and Geology.
624 Slim, M., J. T. Perron, S. J. Martel, and K. Singha (2015), Topographic stress and rock
625   fracture: a two-dimensional numerical model for arbitrary topography and
626   preliminary comparison with borehole observations, *Earth Surface Processes and*
627   *Landforms*, *40*(4), 512-529.
628 Trabucco, A., and R. Zomer (2019), *Global Aridity Index and Potential Evapotranspiration*
629   *(ET0) Climate Database v2. CGIAR Consortium for Spatial Information*
630 *(CGIAR-CSI). Published online, available from the CGIAR-CSI GeoPortal at*
631   *https://cgiarcsi.community*.
632 Wakabayashi, J., and T. L. Sawyer (2000), Neotectonics of the Sierra Nevada and the Sierra
633   Nevada-Basin and Range transition, California, with field trip stop descriptions for
634   the northeastern Sierra Nevada, in *Field Guide to the Geology and Tectonics of the*
635   *Northern Sierra Nevada*, edited by E. R. Brooks and L. T. Dida, pp. 173 - 212,
636   California Division of Mines and Geology.
637 Wood, R. (2013), Transient hillslope response to an incision wave sweeping up a watershed:
638   a case study from the Salmon River, MS thesis, 42 pp, San Jose State University, San
639   Jose, CA.
640

641

642

643   Figure captions

644   **Figure 1.** Map of the United States showing the locations of the study sites.

645

646   **Figure 2.** Median hilltop curvature increases with the approximate square root of erosion

647   rate. Because ridgetops have negative curvature, the absolute value of curvature is plotted to

648   allow a power-law regression. For clarity, error bars are not shown here; uncertainties are

649   presented in Table 1.

650

651   **Figure 3.** Corrected median hilltop curvature vs. erosion rate. Accounting for grid-resolution

652   effects modifies the relationship between curvature and erosion rate, albeit only slightly

653   (compare with Figure 2).

654

655   **Figure 4.** Inferred transport efficiency (D) increases approximately with the square root of

656   erosion rate. D was calculated using the corrected hilltop curvatures.

657

658   **Figure 5.** Inferred transport efficiency (D) vs. various climatic measures. Inferred transport

659   efficiency does not depend significantly on mean annual precipitation (A), mean annual

660   temperature (B), or the aridity index (C). Note that the plot for mean annual temperature does

661   not include the data set from Richardson et al. [2019], which did not provide these values.

662

663   **Figure 6.** Geometric mean of particle size (R) increases with inferred erosion rate (E) at the

664   Feather River site [*Gabet et al.*, 2015]. Particle sizes of soil surface samples were measured

665   at regular intervals along a ridge with a gradient in erosion rates. Because local topography

666 along the ridgeline (i.e., saddles and knobs) was found to have a strong control on soil

667 properties at this site, we present here only the data from the knobs. Erosion rate calculated

668 from ridgetop curvatures using the relationship reported in the present study. 1σ for particle

669 size data averages 5.8 mm (error bars not shown for clarity).

670

671 **Figure 7.** Mean slope at the ridgeline increases with erosion rate. The steeper slopes

672 generally found in rapidly eroding landscapes can also be recognized along the ridgecrests.

673

674 **Figure 8.** Product of hilltop curvature and slope vs. erosion rate. The nearly linear

675 relationship between the two supports a sediment flux law of the form $q_s = KS^2$. This linear

676 relationship may be a mathematical artefact.

677

678 **Figure 9.** Comparison of nonlinear sediment flux equations. Dashed line represents the

679 commonly used nonlinear equation calibrated with values determined in Roering et al.

680 [1999]. Solid line represents fluxes calculated with Eqn. (11b) and calibrated to provide a

681 comparison with the dashed line. Fluxes were calculated over the range of hilltop gradients

682 measured at our field sites. Note that a linear regression (not shown) through the dashed line

683 yields an R^2 of 0.9999, confirming the use of Eqn. (1) as an appropriate substitute for the

684 standard nonlinear equation at low slopes.

685

686 **Figure 10.** Curvature vs. erosion rate according to rock type. For the same erosion rate, the

687 hilltop curvature is lower at sites underlain with presumably weaker bedrock when compared

688 to sites with stronger bedrock. Sites shown with the square markers are Tennessee Valley

689   (CA), Oregon Coast Range (OR), Gabilan Mesa (CA), and Allegheny Plateau (PA) [*Perron*

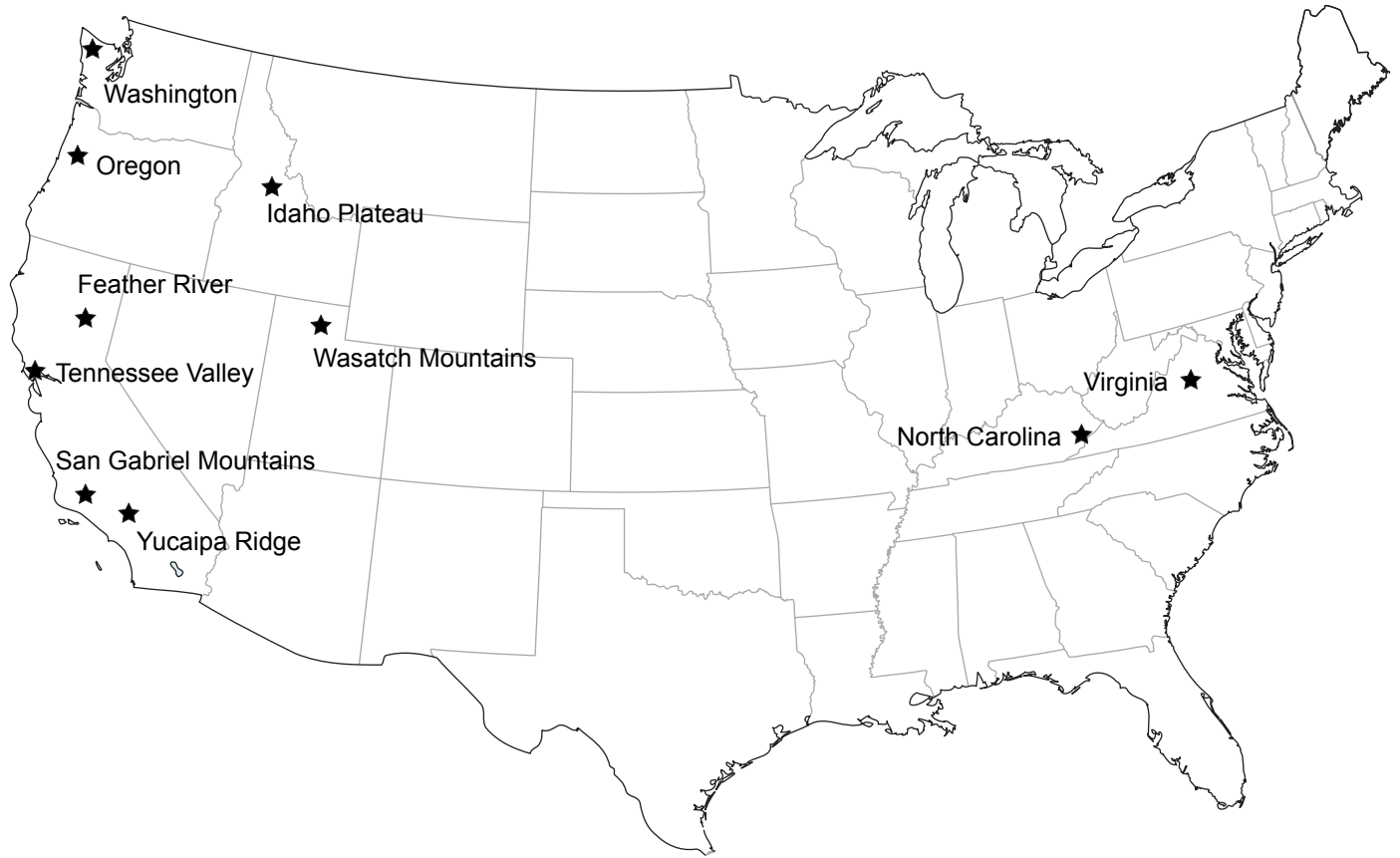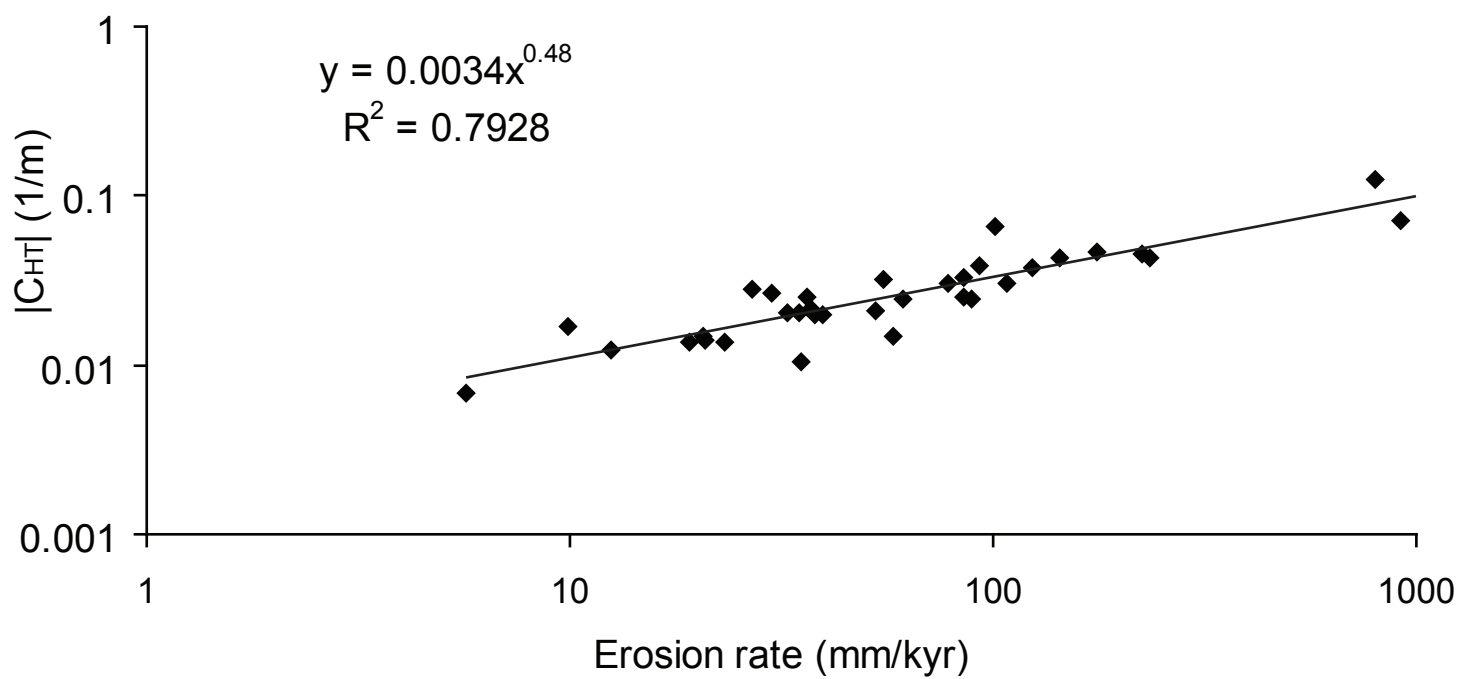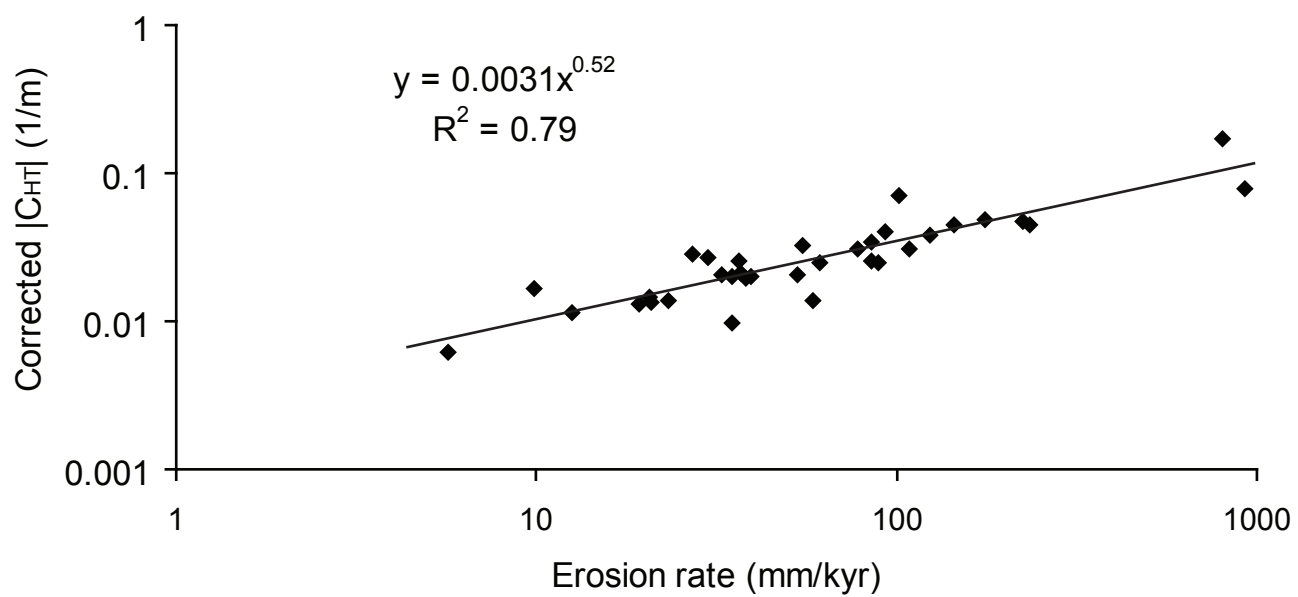690   *et al.*, 2012; *Richardson et al.*, 2019].

691
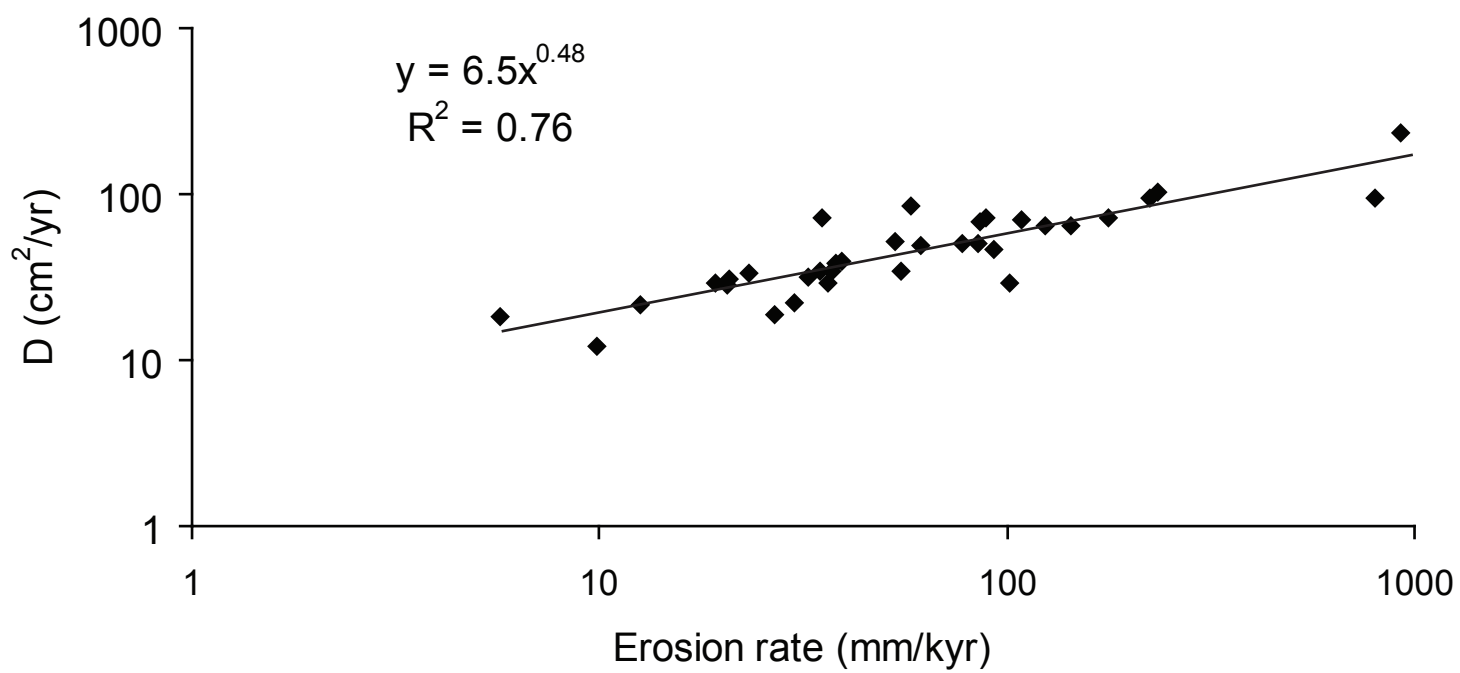
Figure 1.

Figure 2.

Figure 3.

Figure 4.

$y = 6.5x^{0.48}$

$R^2 = 0.76$

Figure 5.

(A)

y = 0.06x + 47
R^2 = 0.01

D (m^2/yr)

Mean annual precipitation (cm/yr)

(B)

y = 64 - x
R^2 = 0.01

D (m^2/yr)

Mean annual temperature (^{o}C)

(C)

y = -13x + 56
R^2 = 0.01

D (m^2/yr)

Aridity Index
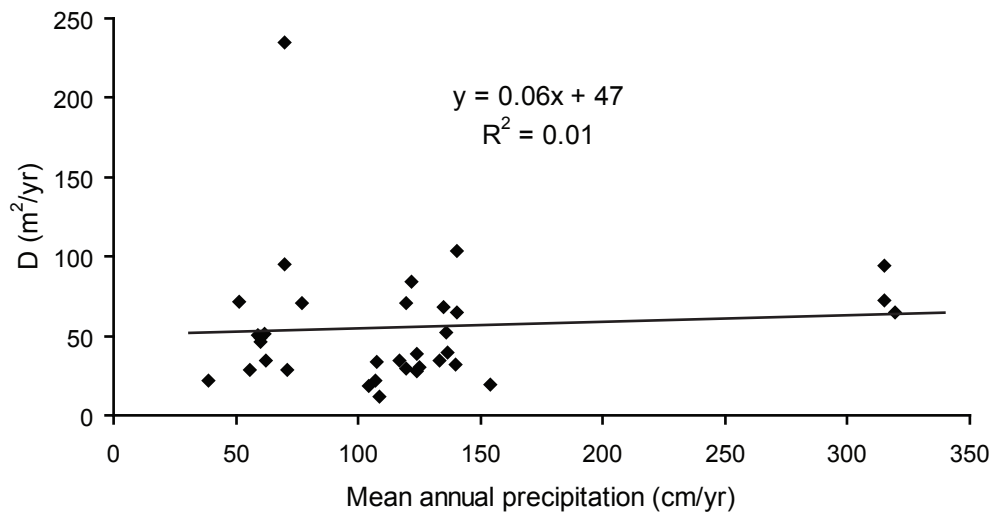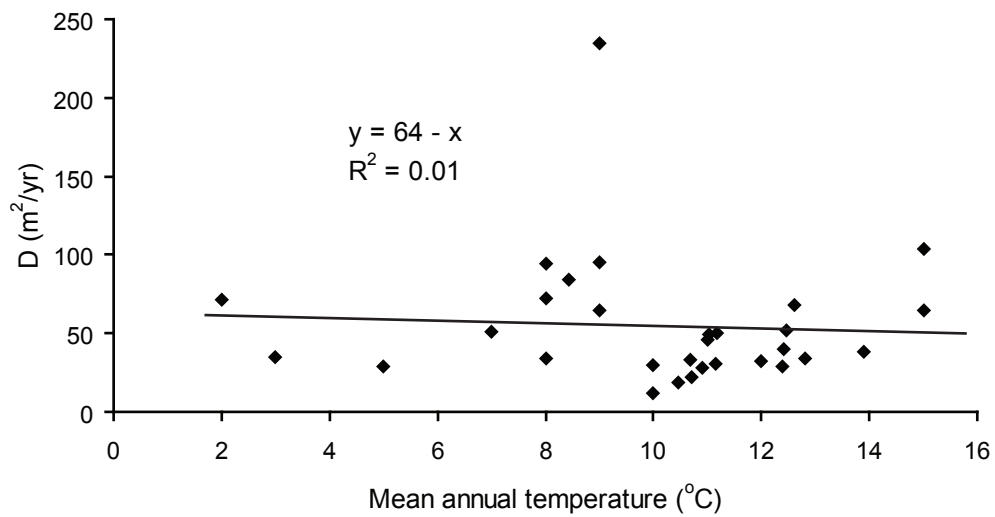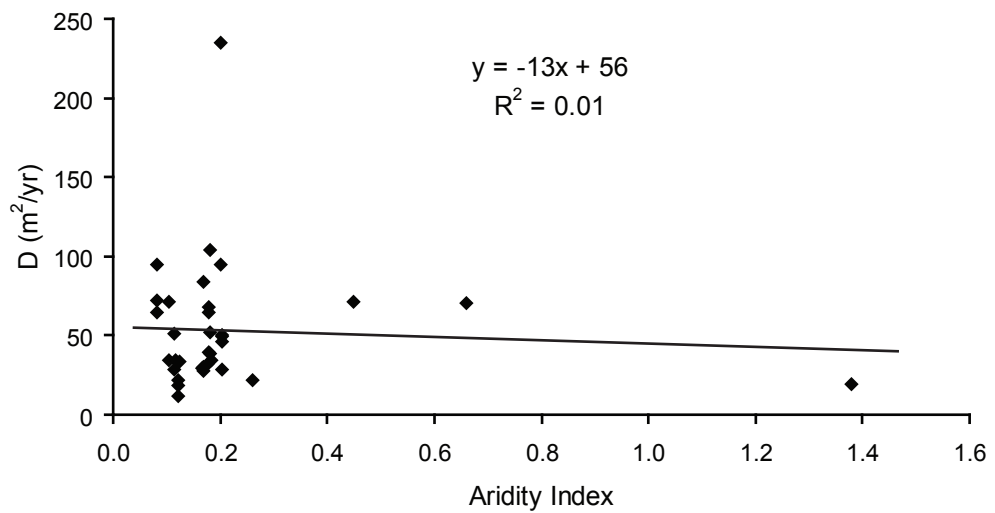
Figure 6.

Figure 7.

Figure 8.

$$y = (1.3 * 10^{-5})x^{1.00}$$
$$R^2 = 0.82$$

Y-axis: $C_{HT}*S_{HT}$ (m/m²)

X-axis: Erosion rate (mm/kyr)

Figure 9.

$q_s = KS/[1-(S/S_c)^2]$
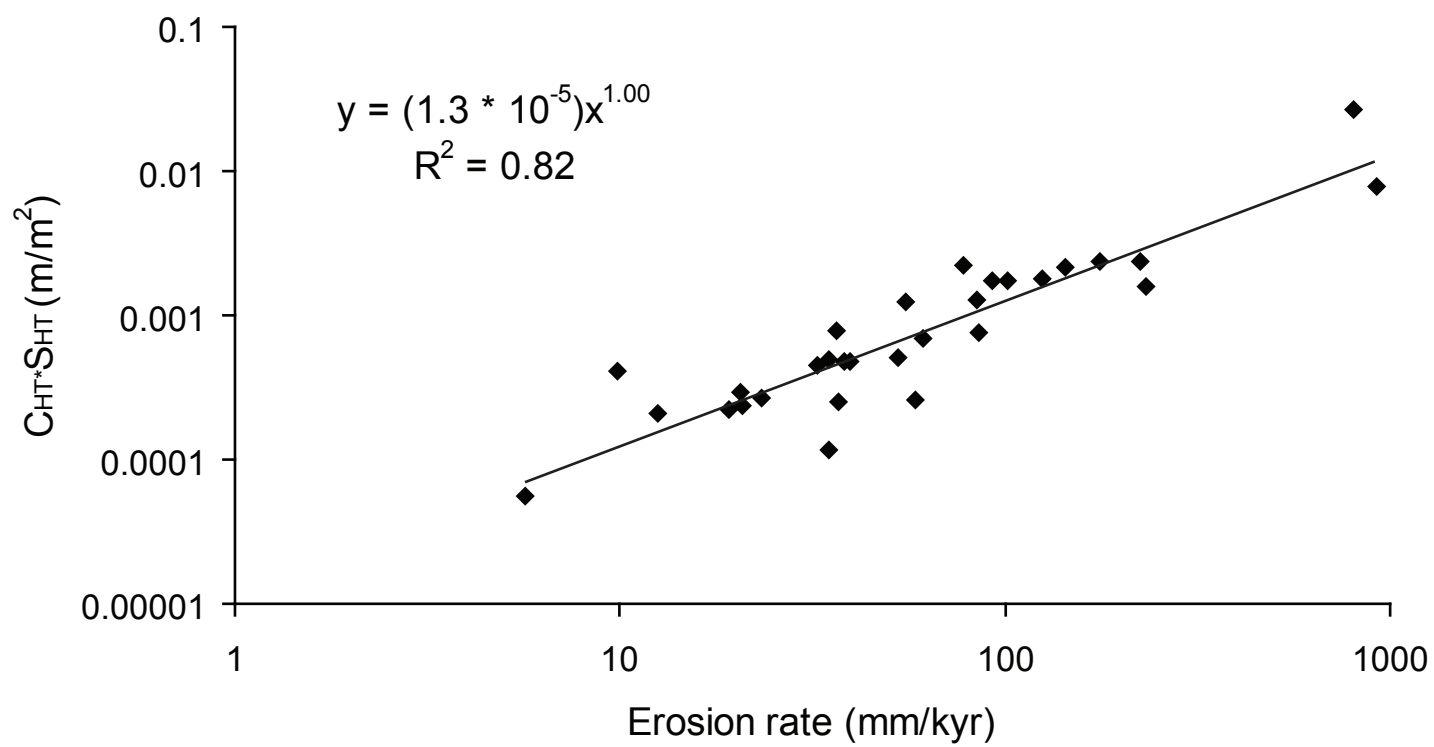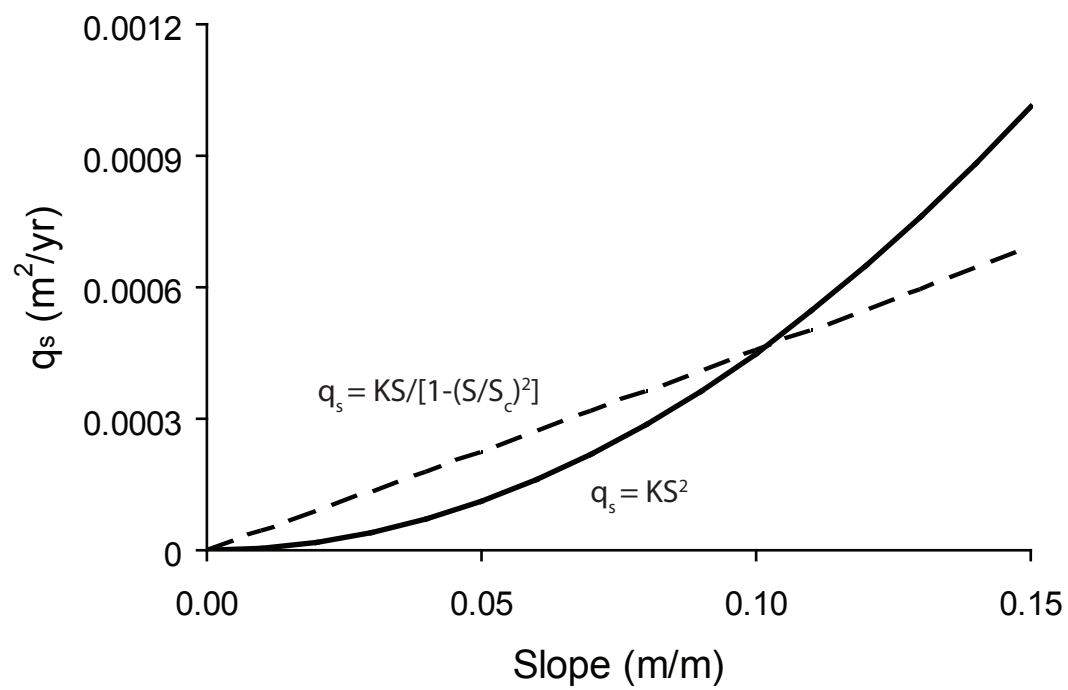
$q_s = KS^2$

q_s (m^2/yr)
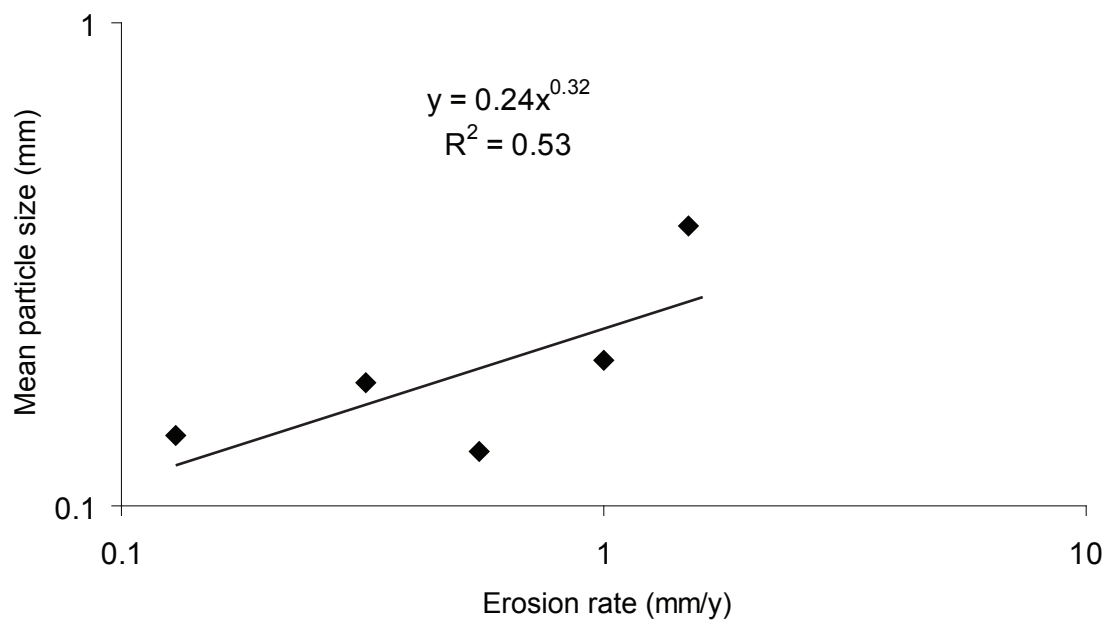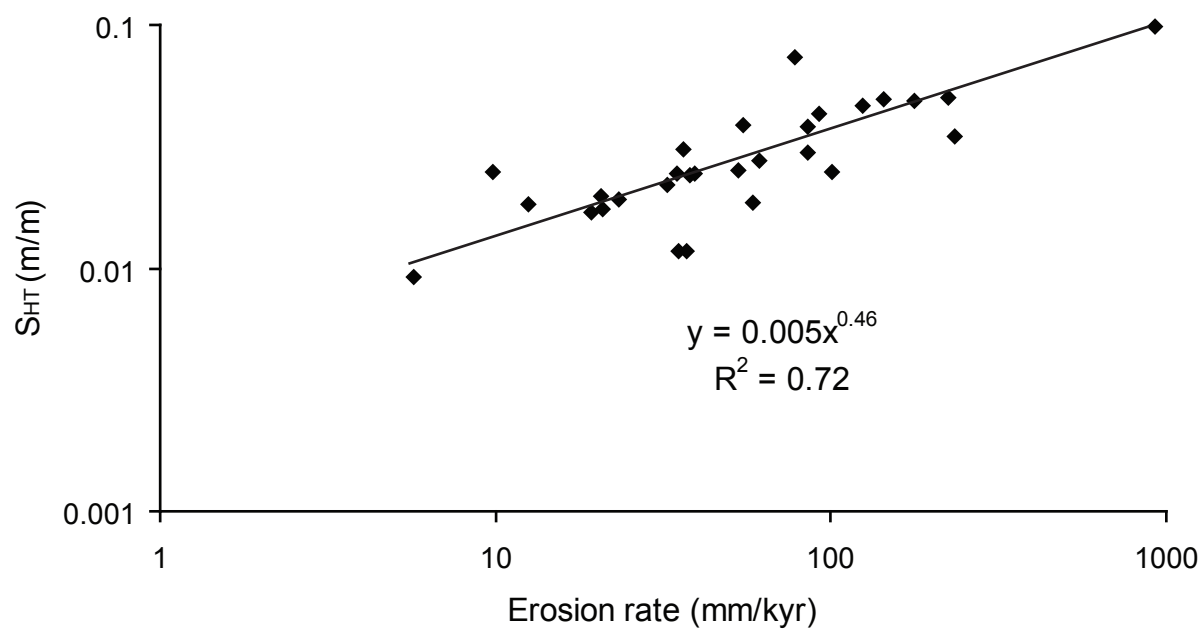
Slope (m/m)

Figure 10.
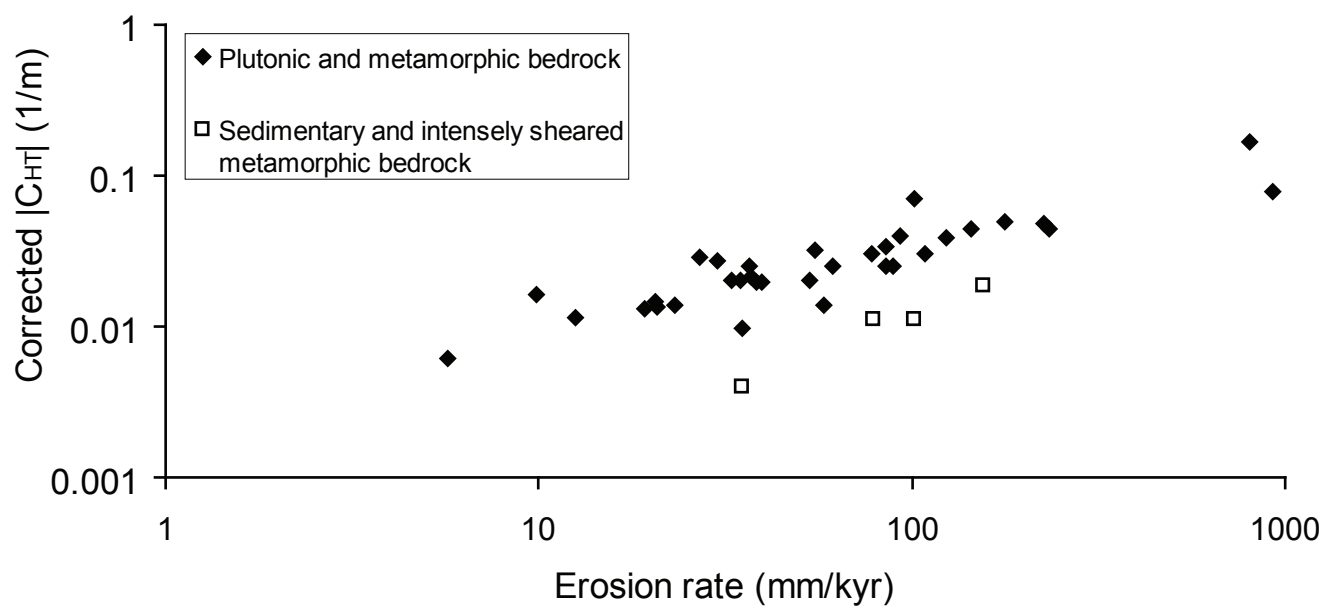
Table 1. Site information. (na = not available)

Region	Source	Sample ID	Latitude (°N)	Longitude (°W)	Lith-ology[j]	MAT[k] (°C)	MAP[k] (cm/yr)	Eros. ± 1σ (mm/kyr)	Med. Crv.[l] (1/m)	Ave. Slope (m/m)	D[l] ± 1σ (cm^2/yr)
San Gabriel	a	SG128	34.3376	118.0104	gr	12	55.5	37 ± 8	-0.02544	0.031	29 ± 6
Mountains	a	SG130	34.3783	117.9893	gr	11	59.8	62 ± 13	-0.02515	0.028	50 ± 10
(CA)	a	SG131	34.3666	117.9920	gr	11	58.8	85 ± 20	-0.03410	0.038	49 ± 12
	a	SG132	34.3658	117.9891	gr	11	60.1	93 ± 19	-0.04039	0.043	46 ± 9
	b	na	34.3640	117.9920	gr	na	77.1	108 ± 17	-0.03086	na	70 ± 12
Idaho Plateau	c	S1	45.4773	114.9618	tnlt	8	62.4	55 ± 11	-0.03254	0.039	34 ± 7
(ID)	c	S2	45.5008	114.9519	tnlt	5	71.0	101 ± 21	-0.07189	0.025	28 ± 7
	c	S3	45.5262	114.9293	tnlt	3	116.6	37 ± 7	-0.02139	0.012	34 ± 7
	c	R2	45.4843	114.9558	tnlt	7	61.8	78 ± 16	-0.03083	0.073	51 ± 11
	c	R3	45.5348	114.9015	tnlt	2	119.8	35 ± 7	-0.00971	0.019	72 ± 14
Yucaipa Ridge	d	3	34.0497	116.9280	qm, gns	9	70.1	922 ± 203	-0.08083	0.092	228 ± 57
(CA)	d	4	34.0530	116.9401	qm, gns	9	70.1	801 ± 175	-0.18688	0.159	86 ± 28
Blasingame (CA)	b	na	36.9540	119.6310	tnlt	na	38.7	30 ± 4	-0.02727	na	22 ± 3
Olympic	e	U-WC-S	47.7399	124.0457	gw	8	315.1	177 ± 39	-0.04884	0.049	72 ± 17
Peninsula (WA)	e	L-WC-S	47.7302	124.0379	gw	8	315.1	225 ± 51	-0.04755	0.050	95 ± 22
	e	L-EFMC-S	47.6581	124.2432	gw	9	319.6	144 ± 34	-0.04422	0.049	65 ± 16
Blue Ridge	f	SH-01a	38.5713	78.2873	gr	11	107.5	23 ± 5	-0.01391	0.019	33 ± 7
Mountains	f	SH-02a	38.6636	78.3550	mb	10	104.5	6 ± 1	-0.00616	0.009	19 ± 4
(VA)	f	SH-07	38.5816	78.4144	gr	10	108.6	10 ± 2	-0.01699	0.025	12 ± 2
	f	SH-10	38.6572	78.2822	gr	11	106.8	13 ± 3	-0.01203	0.018	21 ± 5
Feather River	g	BRB-2	39.6491	121.3020	qd	12	140.0	33 ± 7	-0.02036	0.022	32 ± 7
(CA)	h	BEAN-1	39.6126	121.3295	qd	13	133.2	35 ± 8	-0.02013	0.024	35 ± 7
	h	BEAN-2	39.6225	121.3283	qd	14	124.0	38 ± 8	-0.01969	0.024	39 ± 8
	h	BEAN-4	39.6237	121.3273	qd	12	136.1	53 ± 12	-0.02097	0.025	51 ± 11
	h	BEAN-5	39.6312	121.3298	qd	13	136.5	40 ± 8	-0.01954	0.024	40 ± 8
	i	BEAN-7	39.6284	121.3277	qd	13	134.7	85 ± 18	-0.02557	0.030	67 ± 14
	i	FT-3	39.6714	121.3109	qd	11	123.7	21 ± 4	-0.01425	0.017	29 ± 6
	i	FT-4	39.6712	121.3109	qd	11	124.8	21 ± 4	-0.01513	0.020	27 ± 6

	i	FT-6	39.6784	121.3155	qd	10	119.8	19 ± 4	-0.01338	0.017	29 ± 6
	i	SB-1	39.7189	121.2411	qd	8	121.9	58 ± 12	-0.01475	0.019	79 ± 17
	i	FR-4	39.6344	121.2771	qd	15	140.5	234 ± 79	-0.04535	0.035	103 ± 36
	i	FR-5	39.6354	121.2713	qd	15	140.5	124 ± 39	-0.03858	0.047	64 ± 21
Wasatch Mtns (Utah)	b	na	40.8920	111.8650	gr	na	51.5	89 ± 9	-0.02507	na	71 ±15
Great Smokey Mtns (NC)	b	na	35.6220	83.2040	qtz	na	154.0	27 ± 2	-0.02872	na	19 ±1

[a] Source for [10]Be data and lithology: [*DiBiase et al.*, 2010]

[b] Source for all data: [*Richardson et al.*, 2019]

[c] Samples were collected for this study; source for lithology: [*Wood*, 2013]

[d] Source for [10]Be data and lithology: [*Binnie et al.*, 2007]

[e] Source for [10]Be data and lithology: [*Belmont et al.*, 2007]

[f] Source for [10]Be data and lithology: [*Duxbury*, 2009]

[g] Source for [10]Be data for all Feather River samples except FR-4 and FR-5: [*Hurst et al.*, 2012]

[h] Source for [10]Be data for FR-4 and FR-5: [*Riebe et al.*, 2001]

[i] Source for lithology: [*Saucedo and Wagner*, 1992]

[j] gr = granitic, tnlt = tonalite, qm = quartz monzonite, gns = gneiss, gw = greywacke, mb = metabasalt, qd = quartz diorite, qtz = quartzite

[k] applies to data from all sources except Richardson et al [2019]; MAT = mean annual temperature; MAP = mean annual precipitation; data from the PRISM Climate Group, http://prism.oregonstate.edu, accessed 25 March 2017

[l] Values corrected for grid-resolution effects. Grid-resolution adjustment for sites L-WC-S, L-EFMC-S, SH-01a, SH-02a used a 12-m analysis window because adustments using 14-window failed to converge to a solution. Sensitivity analyses indicate an average difference of <2% for curvature corrections using a window diameter of 12 m vs. 14 m.

Table 2. Details of ^{10}Be analysis from Idaho site.

Sample ID	Sample depth intervals (cm)	AMS measurement ID	^{10}Be concentration ($\times 10^3$ at g^{-1})	^{10}Be concentration uncertainty 1σ ($\times 10^3$ at g^{-1})
S1	0 - 2	s04446	119.9	5.7
S2	8 - 10	s04447	91.94	7.18
S3	16 - 18	s04448	373.7	17.8
R2	n/a	s04450	91.49	4.43
R3	n/a	s04451	408.8	15.1
R4	n/a	s04452	480.1	16.6